

Interconnected Metallic Membrane Enabled by MXene Inks Toward High-Rate Anode and High-Voltage Cathode for Li-Ion Batteries

Chuanfang (John) Zhang,^{a,*#} Wengao Zhao,^{b,c,*#} Sang-Hoon Park,^{d, e#} Tiezhu Guo,^b Shungui Deng,^b Andrés Seral-Ascaso,^d Mayan Si,^b Rabeb Grissa,^b Sebastian Barwich^f and Valeria Nicolosi^d

^a*College of Materials Science & Engineering, Sichuan University, Chengdu, 610065, Sichuan, China*

^b*Swiss Federal Laboratories for Materials Science and Technology (Empa), ETH Domain, Überlandstrasse 129, CH-8600 Dübendorf, Switzerland*

^c*Current affiliation at Institute of Nanotechnology, Karlsruhe Institute of Technology (KIT), 76344 Eggenstein-Leopoldshafen, Germany*

^d*School of Chemistry, Trinity College Dublin, Dublin 2, Ireland*

^e*Advanced Energy Technology R&D Center, Korea Institute of Energy Research, Ulsan 44776, South Korea*

^f*School of Physics, Trinity College Dublin, Dublin 2, Ireland*

*chuanfang.zhang@scu.edu.cn (Chuanfang (John) Zhang)

*wengao.zhao@kit.edu (Wengao Zhao)

These authors contributed equally to this work.

This document is the accepted manuscript version of the following article:

Zhang, C., Zhao, W., Park, S. H., Guo, T., Deng, S., Seral-Ascaso, A., ... Nicolosi, V. (2023). Interconnected metallic membrane enabled by MXene inks toward high-rate anode and high-voltage cathode for Li-Ion batteries. *Advanced Functional Materials*. <https://doi.org/10.1002/adfm.202213860>

Abstract

The ever-increasing popularity of smart electronics demands advanced Li-ion batteries capable of charging faster and storing more energy, which in turn stimulates the innovation of electrode additives. Developing single-phase conductive networks featuring excellent mechanical strength/integrity coupled with efficient electron transport and durability at high-voltage operation should maximize the rate capability and energy density, however, this has proven to be quite challenging. Herein, we show that a two-dimensional titanium carbide (known as MXene) metallic membrane can be used as single-phase interconnected conductive binder for commercial Li-ion battery anode (i.e., $\text{Li}_4\text{Ti}_5\text{O}_{12}$) and high-voltage cathodes (i.e., $\text{Ni}_{0.8}\text{Mn}_{0.1}\text{Co}_{0.1}\text{O}_2$). Electrodes were fabricated directly by slurry-casting of MXene aqueous inks composited with active materials without any other additives or solvents. The interconnected metallic MXene membrane ensures fast charge transport and provides good durability, demonstrating excellent rate performance in the $\text{Li}/\text{Li}_4\text{Ti}_5\text{O}_{12}$ cell (90 mAh/g at 45 C) and high reversible capacity (154 mAh/g at 0.2C/0.5C) in $\text{Li}/\text{Ni}_{0.8}\text{Mn}_{0.1}\text{Co}_{0.1}\text{O}_2$ cell coupled with high-voltage operation (4.3 V vs Li/Li^+). The LTO//NMC full cell demonstrates promising cycling stability, maintaining capacity retention of 101.4% after 200 cycles at 4.25 V (vs Li/Li^+) operation. This work provides insights into the rational design of binder-free electrodes toward acceptable cyclability and high-power density Li-ion batteries.

Keywords: MXene inks, Li-ion battery, high-rate, high-voltage, binder-free

Introductions

Utilization of Li-ion chemistry to store the electrochemical energy can address the ever-increasing demands from portable electronics and hybrid electric vehicles.^[1-4] Such tough challenges to battery safety and lifetime issues require high-performance battery components, focusing mainly on electrodes or electrolytes with novel nanostructures and chemistries.^[5-8] It is worth noting that the development of electrode additives is also significant, as it plays a crucial role in maintaining the electrode's conductive network and mechanical integrity.^[9-11]

Traditionally, electrode additives are made of dual-component based on a conductive agent (i.e. carbon black, CB) and a polymeric binder. While the former ensures the charge transport throughout the electrode, the latter mechanically holds the active materials and CB for close electrical contact during cycling.^[12-14] Although these traditional electrode additives have been widely applied in Li-ion battery technologies, they cannot maintain the microstructure of the electrode composite, especially while the electrode experiences large volume variations.^[15] This is because the polymeric binder cannot completely prevent the contact loss between the active material and conducting agent upon repeated lithiation/delithiation, thus leading to severe disruption of the conducting networks.^[16-18] Moreover, the required amounts of dual-component additives also increase the inactive mass of the battery electrode, which compromises the gravimetric capacity per electrode and device.^[19]

These issues can be solved by replacing the dual-component additives with individual compound that provides electrical conductivity and mechanical integrity, the so-called dual-functionality conductive binder.^[20-22] Compared to the conventional electrodes with dual-component additives, electrodes based on conductive binders possess improved electrical contacts and enhanced mechanical adhesion, ensuring excellent charge propagation/transport kinetics and electrode structural integrity upon repeated “breathing” of active materials. In

addition, since conductive binders only contain one sole additive, the total amount of inactive volume/mass is decreased, leading to an improved battery gravimetric/volumetric capacity. It's worth noting that, by formulating conductive binders into viscous inks, one can expect a straightforward electrode fabrication upon the direct casting of the composited homogeneous slurries-procedures that are highly compatible with the industrialized battery electrode production line. Inks based on carbon nanotubes, reduced graphene oxide,^[23] poly(3,4-ethylenedioxythiophene),^[24] poly(styrenesulfonic acid),^[25] polyaniline (PANi),^[26] and polypyrrole (PPy)^[27] etc., have been reported as conductive binders of anodes or cathodes in Li-ion battery. However, these conductive binders either showcase unsatisfied electronic conductivity and/or mechanical strength, limiting the rate capability and cycling stability of resultant electrodes. Moreover, the critical cracking thickness (CCT) of the conductive binder-based slurries (i.e. conductive polymer solutions) is typically low (due to the fairly low viscosity or the high capillary pressure in the slurry drying process), which dramatically reduces the achievable mass loading and areal capacity of the conductive polymer binder-based electrodes.^[28, 29] This means that formulating novel conductive binder inks with excellent conductivity and impressive mechanical toughness coupled with high viscosities, is quite essential and urgent.

On the other side, while most conductive binders were studied for high-theoretical-capacity anodes such as Si, much fewer reports on the conductive binders-enabled high-rate anode and high-voltage cathodes are available.^[30-32] We note that driving the high-voltage cathode operation is equally important to match the high energy density of Si-based anode in LIBs. Moreover, engineering a highly stable anode featuring high-rate response is also significant in exploring fast charging yet safe batteries. However, to the best of our knowledge, it's been proven to be quite challenging to develop conductive binders that are simultaneously applicable for high-rate, stable anodes, and high-voltage cathodes.

Herein, we demonstrate that the abovementioned goals can be simultaneously reached by exploring titanium carbide ($\text{Ti}_3\text{C}_2\text{T}_x$, T_x represents terminations) MXene aqueous inks as a new class of conductive binders. MXenes, with a general formula $\text{M}_{n+1}\text{X}_n\text{T}_x$ ($n=1-4$), are produced by chemically etching the A-site element (such as Al, Ga) from the MAX phase (where M is an early transition metal, X is carbon and/or N), leaving abundant hydrophilic groups ($-\text{OH}$, $-\text{O}$, $-\text{F}$) terminated on the M surface (T_x).^[33-36] We utilize the outstanding electrical conductivity and excellent mechanical toughness/strength of $\text{Ti}_3\text{C}_2\text{T}_x$ MXene to facilitate the formation of an interconnected metallic nanosheet network. Such a robust conductive network allows fast charge distribution and maintains electrode integrity upon repeated charging-discharging, enabling high-rate $\text{Li}_4\text{Ti}_5\text{O}_{12}/\text{Ti}_3\text{C}_2\text{T}_x$ (labelled as LTO/MX) anode and high-capacity, high-voltage $\text{LiNi}_{0.8}\text{Mn}_{0.1}\text{Co}_{0.1}\text{O}_2/\text{Ti}_3\text{C}_2\text{T}_x$ (labelled as NMC/MX) cathode, as shown in **Scheme 1**. The Li//NMC/MX cell delivers a capacity of 154 mAh g^{-1} and maintains a retention of 81% after 300 cycles in the high-voltage operation of 4.3V (vs Li/Li^+). The full cell based on LTO/MX and NMC/MX does not exhibit a capacity decay after 200 cycles, indicating the great potential of MXene inks in realizing high-energy, high-power Li-ion batteries with stable cycling performance. This work may further stimulate the in-depth study of electrode additives for the scalable production of high-performance battery electrodes.

Results

MXene inks formulation and characterizations

We start by describing the $\text{Ti}_3\text{C}_2\text{T}_x$ MXene (labelled as MX in figure panels) inks formulation. The MX phase precursor, which shows the typical morphology of layered ceramics according to the scanning electron microscopy (SEM) images (Supplementary Figure 1a), was immersed in hydrochloric acid (HCl)-lithium fluoride (LiF) solution.^[37, 38] After the complete reaction, particles with apparent gaps among sheets were obtained, indicating successful etching and

preparation of multi-layered MX (Supplementary Figure 1b).^[39] By repeatedly exchanging the intercalated Li^+ with deionized water followed by vigorous manual shaking, the multi-layered MX swelled and delaminated into predominantly single-layer MX flakes.^[36, 40] By cascading the flakes via centrifugation, concentrated MX aqueous ink was obtained, as shown in **Figure 1a**. The ink, with a concentration up to 40 mg/mL, is consisted of clean MX flakes with smooth surfaces and well-defined edges.^[41] In addition, no needle-like chunks are observed, indicating the minimum oxidation over the etching-delamination-ink formulation procedures (Figure 1b). These flakes possess a hexagonal atomic structure agreeing well with previous reports (inset in Figure 1b).^[37, 42] The atomic force microscopy and the corresponding height profiles in Figure 1c further confirm the presence of predominantly single-layer MX flakes, as most of delaminated nanosheets with 1.7 nm in thickness were observed. This thickness is higher than the pristine MX flakes (~ 1.0 nm), which can be attributed to the surface adsorption of water and/or the terminations.^[40] The statistics histogram indicates a mean flake lateral size of 1.4 μm (Figure 1d).

Since the electrode fabrication highly depends on the viscosity of the composite slurry, it's essential to understand the rheological behaviours of the as-formulated MX inks. Here the suspensions based on CB/PVDF/NMP and PVDF/NMP were also formulated (with the same solid fraction) and evaluated. As shown in Figure 1e, all samples exhibit shear-thinning behaviour with non-Newtonian characteristics, which can be well explained using the Ostwald-de Wael power law.^[43, 44] The viscosity of MX ink is much higher than that of CB/PVDF/NMP system (or PVDF/NMP system) in the full range of shear rate and can be well attributed to the much higher surface to volume ratio in MX nanosheets.^[39] Apart from the viscosity, the viscoelastic properties (particularly storage modulus, G' and loss modulus, G'') of the slurries also provide valuable information on the sample fluidisation and give insights into the structural integrity after the shear force is removed.^[45] As shown in Figure 1f, the MX aqueous

inks exhibit the highest G' and G'' , followed by CB/PVDF/NMP and PVDF/NMP systems. We note that formulating slurry with high G' and G'' is significant in fabricating robust, smooth electrodes without forming cracks upon drying. Besides, slurries with high G' and G'' allow the direct casting of high mass loading electrodes. This is well evidenced by the electrode fabrication in Figure 1g, as LTO/MX, LFP/MX and NMC/MX viscous homogeneous slurries were blade-coated on respective current collectors without additional CB/binders/solvents. No cracks are observed after drying; all electrodes showcase a smooth surface and nicely adhered to the current collectors.

Electrode characterizations

To further examine the role of MX nanosheets in maintaining the electrode structural integrity, scanning electron microscopy (SEM) studies were performed. Top-view and cross-sectional SEM images indicate that LTO nanoparticles are well embedded in the matrix of MX metallic network (Supplementary Figure 2), which guarantees fast electron transport kinetics as well as preserving the electrode stability. A closer examination confirms that LTO nanoparticles are homogeneously wrapped by the MX nanosheets (**Figure 2a**), suggesting good contact between LTO and MX, substantially minimized the electrical polarization in batteries. No phase changes of MX or LTO are observed during the electrode fabrication based on the X-ray diffraction (XRD) patterns and Raman spectra (Supplementary Figure 3a, b).

Similarly, LFP nanoparticles are also tightly encapsulated by the robust MX conductive membrane (Figure 2b, top panel), forming a sandwiched architecture with interconnected metallic skeleton to transport electrons to the current collector (Figure 2b, bottom panel). Such a sandwiched morphology is more apparent in the NMC/MX electrode, where the NMC microparticles are compactly covered by the continuous metallic MX membrane (Figure 2c). We note that the as-formed interconnected MX membrane not only ensures good electrical

contact (in a point-to-plane manner) between the abovementioned active materials and MX sheets, but also plays a significant role in assimilating electrode stress/strain, leading to a robust electrode with improved structural stability. This contrasts sharply with the conventional LTO/CB/PVDF electrode, which showcases a fluffy morphology with point-to-point contact between LTO and CB (Supplementary Figure 4). Such an electrical contact behaviour in the conventional electrode may lead to higher charge-transfer resistance due to plenty of junctions, potentially compromising the rate handling properties, as discussed below.

Electrical and mechanical characterization

To check if the introduction of MX has indeed improved the electrical properties of the resultant electrodes, four-point-probe electrical conductivity was employed to measure MX-based electrodes and the corresponding electrodes with dual-component additives. Figure 2d implies that by adding 10 wt% MX nanosheets to the LTO nanoparticles, the conductivity of LTO/MX (2000 S/m) has been dramatically increased by ~ 1000 times and ~ 200 times compared to the traditional systems-LTO/CB/PVDF with 80:10:10 and 90:5:5 in weight ratio, respectively. For LFP/MX (810 S/m) and NMC/MX (150 S/m), the electrode conductivity has improved by ~ 400 times and ~ 15 times from their respective counterpart (with 80:10:10 in weight ratio), demonstrating the unique advantage of employing MX as a conductive binder in improving the electrode electrical conductivity. In addition, the conductivity of LTO/MX remains almost consistent upon repeated bending (Figure 2e), similar to the response of pure MX film (4500 S/cm). The excellent electrical conductivity and robust nature of the LTO/MX electrode can be well attributed to the resilient interconnected MX metallic membrane, as well as the point-to-plane contact behaviour which ensures efficient charge transport and structural stability even in a twisted configuration (top panel, Figure 2e).

To further clarify the mechanical reinforcement the MX conductive binders enabled, the stress-strain curves of LTO/MX, pure MX, and LTO/CB/PVDF strips (obtained by blade coating) were measured.^[39] As shown in Figure 2f-g, the tensile toughness and Young's modulus have been improved to 1.1 kJ m⁻³ and 269 MPa, respectively, in the LTO/MX from the conventional LTO/CB/PVDF electrode at the equivalent composition (80 wt% of LTO, 0.4 kJ m⁻³, and 74 MPa). The enhanced mechanical properties correspond to a larger CCT than that of traditional binder-based system, suggesting that the as-formulated MX aqueous viscous inks may be employed to construct electrodes with high mass loading and high areal capacity anodes and cathodes. It's also worth noting that these improved properties were obtained based on MX flakes with a relatively small lateral size (1.4 μ m). It's reasonable to expect further substantial improvements in electrical conductivity and mechanical toughness by synthesizing ultra-large flakes (>20 μ m), and formulating into viscous inks with very high G' and G''. As such, ultrathick, robust electrodes with high areal capacity are enabled coupled with advanced electron transport network and mechanical flexibility, which are highly demanded for future wearable power sources. However, formulating ultra-large MXenes viscous ink and therefore, high mass loading anode/cathode are beyond the scope of this work.

Electrochemical characterizations of LTO/MX anodes

The advantages in electrical and mechanical properties brought by the dual-functionalized MXene network should render LTO/MX anode as well as LFP/MX and NMC/MX cathodes with good charge storage performance. We begin by measuring the electrochemical responses of LTO/MX electrodes. The galvanostatic charge-discharge (GCD) curves of LTO/MX and traditional electrodes with different compositions are shown in **Figure 3a**. The 1st Coulombic efficiency (CE) of all electrodes is between 78-81% (Supplementary Figure 5a-b). LTO exhibits a typical voltage plateau around 1.55 V at 0.1 C (1C = 172 mA g⁻¹). The GCD polarization, defined as the gap between charge and discharge plateaus and becomes apparent

with the increase of current density (C-rate). Moreover, compared to the dual-component additive-based electrodes, LTO/MX demonstrates the smallest GCD polarization, followed by traditional electrodes with 10 wt% and 5 wt% CB, respectively, in a trend of electrode's conductivity (Figure 2d). The GCD polarization further highlights the advantages of metallic MX membrane in improving the reaction reversibility of LTO/MX anode. Despite all electrodes exhibit similar specific capacities at 0.1 C, fast capacity decay is observed in these LTO/CB/PVDF electrodes as elevating the charging-discharging rate beyond 1 C, and only retaining 125 mAh/g and 85 mAh/g at 10 C for the 10 wt% CB and 5 wt% CB electrodes, respectively (Supplementary Figure 6). In sharp contrast, LTO/MX still delivers 128 mAh/g at 30 C and then drops to 90 mAh/g at 45 C (Figure 3b), which is limited by the out-of-plane conductivity of the electrode.^[46] The much-improved rate capability in the LTO/MX can be reasonably attributed to the interconnected nanosheet network, which guarantees efficient charge distribution and promotes the ion diffusion kinetics in the sandwiched architecture.

The cycling stabilities of LTO-based electrodes were measured at 5 C (Figure 3c). Unsurprisingly, the LTO/MX retains the highest capacity (150 mAh/g) after 100 cycles corresponding to a capacity retention of 97%, which has dramatically outperformed those of LTO/CB/PVDF electrode. Typical GCD curves at different cycles are compared in Supplementary Figure 7, indicating a gradually decreased reversible capacity and increased GCD polarization in 10 wt% MX-, 10 wt% CB-, and 5 wt% CB-based electrodes, respectively. We attribute the improved specific capacity, rate performance, and cycling stability to the unique design of LTO/MX architecture. Unlike the point-to-point electrical contact between the LTO nanoparticles and CB, the interconnected MX network conformally wrap the LTO, ensuring a point-to-plane contact that avoids the possible phase separation of LTO from MX, and improves the electron transport as well as Li-ion diffusion kinetics.

The cyclic voltammograms (CV) of LTO-based electrodes indicate a gradually increased polarization (the gap between the redox peaks) as enlarging the scan rate (Figure 3d). By plotting the peak current intensity as a function of the root of scan rate (Figure 3e), one is able to derive the Li^+ diffusion coefficient (D_{Li^+}) based on the $i_p = 0.4463mAF(F/RT)^{1/2}C_{\text{Li}}D_{\text{Li}}^{1/2}\omega v^{1/2}$, where i_p is the current peak, m is the number of electrons per reaction, A is the geometric surface area of electrode, F is the Faraday constant (96486 C mol⁻¹), R is the gas constant (8.314 J mol⁻¹ K⁻¹), T is the absolute temperature (K), C_{Li} is the concentration of Li^+ in cathode, and v is the scan rate.^[47] As expected, LTO/MX demonstrates the highest D_{Li^+} up to 6.6×10^{-8} cm²/s, followed by conventional electrodes with 10 wt% CB (4.6×10^{-8} cm²/s) and 5 wt% CB (1.5×10^{-8} cm²/s), respectively (Figure 3f). After cycling, the LTO/MX electrode remains intact with a smooth surface (Figure 3g). This is because the robust MX network well preserves the active materials from losing electrical contact and maintains the electrode integrity. The abundant voids also facilitate Li-ion diffusion, resulting in improved Li^+ diffusion coefficients than traditional LTO-based electrodes (Figure 3h).

The abovementioned results confirm that MX aqueous ink can be used as an efficient conductive binder for high-rate, highly stable Li-ion battery anode. We note that to develop advanced Li-ion batteries, one needs to reshape the cathode so that its electrochemical performance well matches that of the anode (i. e. LTO/MX). Here we use MX aqueous ink to realize high capacity and/or high-voltage cathode, the prerequisite for high-energy-density batteries. It's worth mentioning that reports on high-voltage (>4.0 V) cathodes based on MX as either active material or conductive binders are rare, probably due to the concern that MX nanosheets may be electrochemically oxidized under such a high voltage.

Interestingly, at a similar mass loading, traditional LFP/CB/PVDF electrode shows cracks and peeling off from the Al foil after drying the cast slurry, while the LFP/MX exhibits an intact and smooth electrode surface without apparent cracks, indicative of higher electrode CCT when

using high-aspect-ratio MX nanosheets as conductive binders than that of CB-PVDF dual-component system (**Figure 4a**). The EDX mapping images imply that MX nanosheets are uniformly distributed within the electrode network, serving as interconnected conductive paths while holding the solids together (Figure 4b). GCD curves suggest standard voltage plateaus for LFP with quite small polarization at different C-rate (Figure 4c, top panel). Specific capacity reaches the highest 159 mAh/g at 0.1 C and maintains 133 mAh/g after 70 cycles at 0.3 C (Figure 4c, bottom panel). The top-view SEM image of the LFP/MX electrode indicates that LFP nanoparticles are well sandwiched by the MX conductive binders (Supplementary Figure 8). After cycling, despite the electrode surface is covered by a thin layer of solid-electrolyte-interface (SEI), the electrode structural integrity has been well-preserved thanks to the presence of MX binders (Figure 4d, Supplementary Figure 9,10). The advantages of fabricating high-performance LFP/MX electrodes suggest that MX inks are efficient cathode conductive binders, which may provide suitable alternatives for future electrode additives.

To examine the generality of MX inks for cathode conductive binders, we blended NMC microparticles with MX aqueous inks to fabricate NMC/MX electrodes. NMC microparticles are consisted of plenty of primary particles, forming a sphere-like superstructure morphology (Supplementary Figure 11a). Unlike the conventional NMC/CB/PVDF electrode in which NMC particles loosely contact with CB (Supplementary Figure 11b), the NMC microparticles are uniformly and compactly wrapped by the MX conductive skeleton (Supplementary Figure 12,13). The unique point-to-plane electrical contact between NMC particles and MX binders ensures efficient charge distribution, while the voids created from such a morphology guarantee fast ion diffusion kinetics. Figure 4e suggests the rate performance of NMC/MX electrode from 0.1 C to 10 C. The highest capacity of 154 mAh/g is achieved at 0.1 C, slightly decaying to 130 mAh/g while elevating the C-rate by 10-fold. The cell maintains a capacity of 90 mAh/g at 10 C, demonstrating good rate performance enabled by the highly conductive MX

membrane. The specific capacity recovers to 152 mAh/g as the current density bounds back to 0.1 C after cycling for 35 cycles, demonstrating good reversibility of the redox reactions. The long-term cycling of NMC/MX electrode at 0.5 C indicates that the capacity increases in the first 20 cycles, most probably due to the gradually improved electrolyte penetration, and then slightly decays to 130 mAh/g after 300 cycles (Figure 4f). The first cycle CE of NMC/MX is reasonably high (~87%), and then stabilizes at >99.9% (Figure 4g), suggesting the charging/discharging processes in the high voltage window are reversible. The reversible lithiation/delithiation processes also indicate that the MX conductive network has been well preserved, while the CE deviates and fluctuates under ~99.9%. This is further confirmed from the SEM morphology of post-cycled NMC/MX electrode in Figure 4h, as the homogeneously distributed (from the EDX mapping images) MX conductive binders tightly sandwiched the NMC particles, ensuring the structural integrity (inset) and efficient point-to-plane electrical contact.

To clarify the reasons for the high-voltage NMC/MX with high capacity and good cycling stability, we performed the XPS analysis on NMC/MX electrodes cycled for different times and employed Ar⁺ sputtering to reveal the in-depth composition information. As shown in **Figure 5a**, the TiO₂ peak intensity becomes stronger after cycling for 50 cycles and keeps almost constant after 100 cycles. However, peaks attributed to MX (seen from Ti-C, Ti (II) and Ti (III)) are still present, indicating that MX nanosheets are well preserved. After Ar⁺ sputtering off the top surface layer, the peak intensity ratio of TiO₂ to MX decreases dramatically (Figure 5b), suggesting the MX conductive binders are only oxidized superficially, while the backbone of interconnected MX conductive paths is primarily maintained, ensuring the preservation of electrical conductive paths for efficient charge transport. Indeed, the oxides reach 41.44% on the top surface after 50 cycles, and dramatically reduce to 21.75% (indicating 78.25% carbides have been maintained) after removing the top

surface (Figure 5c). After 100 cycles, the relative percent of oxide/carbide changes slightly, suggesting the electrochemical oxidation of MX has reached a equilibrium and the as-formed surface oxide may work as a protective layer from further electrochemical oxidation. As a result, the robust MX conductive network is retained after cycling, holding NMC particles tightly (Figure 5d). The XRD patterns (Supplementary Figure 14) confirm peaks from NMC and MX. The absence of the oxide peak further suggests that the domain size of surface oxides is relatively small.

Full cell based on LTO/MX anode and NMC/MX cathode

To demonstrate the potential of MX conductive binders for high-performance Li-ion batteries, we assembled a full cell using LTO/MX anode and NMC/MX cathode to evaluate the cycling capability in the voltage of 1.2-2.7 V (2.75-4.25 V vs Li/Li⁺). As shown in Figure 5e, the full cell exhibits a stable cycling life, and the initial capacity has been maintained without apparent decay after 200 cycles at 0.2-0.5 C. The CE is also very stable (>99.9%) throughout 200 cycles. Figure 5f showcases the GCD curve variation at different cycles. While the decay from the 1st to 100th cycle is slight, it becomes visible from 100th to 200th cycle. It is worth noting that this is the first report on MXene conductive binders for stable, high-voltage (4.3 V vs Li/Li⁺) LTO/MX//NMC/MX full cell. Despite the current electrochemical charge storage performance is not the champion among the reported NMC electrodes and full cells, we have enough reasons to believe that the reversible capacity and long-term cycling stability of LTO/MX//NMC/MX full cell can be significantly improved by optimizing the compatibility between MX and cathode/anode. The rapid progress of MX also provides broad members to choose from, with exceptional electrical, mechanical, and electrochemical properties.

Conclusions

To conclude, we report on using MX aqueous inks as a new class of conductive binder for high-rate LTO/MX anode and high-voltage NMC/MX cathode. The interconnected MX metallic network ensures efficient charge propagation and ion diffusion kinetics, but also well assimilates the induced stress during the electrode fabrication and charging/discharging processes, maintaining the electrode structural integrity. Of equal importance is the straightforward electrode formation by utilizing industrially compatible and cost-effective slurry-casting technique, allowing large-scale production of high-performance LTO/MX anode and NMC/MX cathode for batteries. The rapid development of the MX family also paves a promising path to further improve the cyclability and rate capability of MX-base electrodes in LIBs at high-voltage operation.

Methods

The MX viscous ink formulation and characterizations, battery electrode fabrication and cell assembling, as well as the materials characterizations (such as XRD, XPS, Raman, SEM, TEM, etc.), were all documented in detail in the Supplementary file.

Acknowledgements

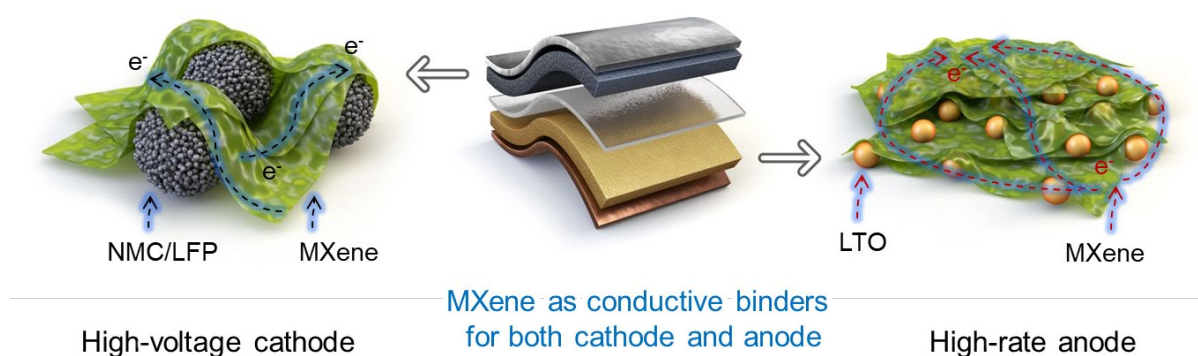
This research was generously supported by “the Fundamental Research Funds for the Central Universities (1082204112A26)”. The authors acknowledge the SFI-funded AMBER research centre (SFI/12/RC/2278) and the Advanced Microscopy Laboratory for the provision of their facilities, as well as Empa microscopy lab. We thank Joao Coelho, Niall McEvoy, Hannah Nerl and Demont Dely for materials characterizations. W.G.Z thanks the battery tester from the lab of Materials for Energy Conversion at EMPA headed by Dr. Corsin Battaglia. We thank Prof. Jonathan N. Coleman and Prof. Yury Gogotsi for helpful discussions. V.N. thanks the European Research Council (StG 2DNanocaps and 3D2D print) and Science Foundation

Ireland (PIYRA) for funding. C.F.Z. thanks the National Natural Science Foundation of China (22209118) as well as Empa internal research funding (Empa-IRC-2019cupsupcap, IRC-2020NifixMX).

Author contributions

C.F.Z. W.G.Z. and S.H.P. contributed equally to this work. C.F.Z., W.G.Z. and S.-H.P. conceived the project. C.F.Z. designed materials and experiments. C.F.Z. and S.G.D. prepared the MXene ink and performed data analysis, C.F.Z., W.G.Z. and S.-H.P. fabricated composite electrodes, W.G.Z. and S.-H.P. performed electrochemical characterization, C.F.Z., W.G.Z., and S.-H.P. analysed electrochemical data, A.S.-A. and S.G.D. performed electron microscopy analysis, C.F.Z. and S.-H.P. measured electrical conductivity, T.Z.G. performed mechanical testing, M. S. and R. G. performed the XPS. S.B. performed the rheology tests, C.F.Z. wrote the manuscript with contributions from W.G.Z. and other co-authors. All authors discussed the results and commented on the manuscript.

Figures



Scheme 1. Scheme of MXene as conductive binders for both high-voltage cathode and high-rate anode. The scheme shows MXene inks as conductive binders for both cathode and anode. The excellent mechanical and electrical properties enabled by the interconnected, resilient MXene nanosheet network ensure excellent charge transport, while simultaneously decreasing the inactive component's weight, resulting in a high-voltage cathode and high-rate anode.

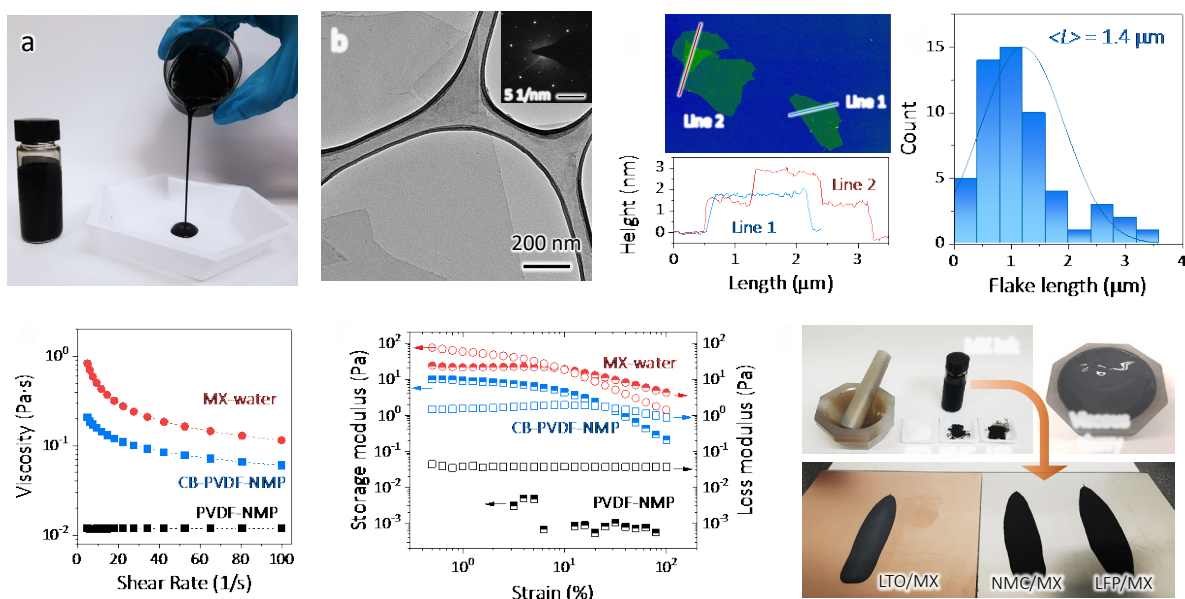


Figure 1. Characterizations on MXene inks. a) An optical image of MXene aqueous viscous inks. b) TEM image of as-synthesized MXene inks with its corresponding selected area electron diffraction (SAED) pattern of the nanosheets shown in the inset. c) AFM image (top panel) and its corresponding height profiles (bottom panel) along lines indicated in the AFM image. d) Histogram of MXene flake lengths obtained *via* TEM statistics. e-f) Rheological properties of MXene inks with e) viscosity plotted as a function of shear rate and f) storage and loss modulus plotted as a function of strain. Also included is the control sample made of PVDF dispersed in NMP with or without carbon black (CB). g) Procedures for cathodes (LFP, NMC) and anode (LTO) fabrication. MXene ink was directly mixed with active materials, forming viscous composite slurries allowing the subsequent blade-coating on metal foils in the absence of additional additives such as CB or polymeric binders.

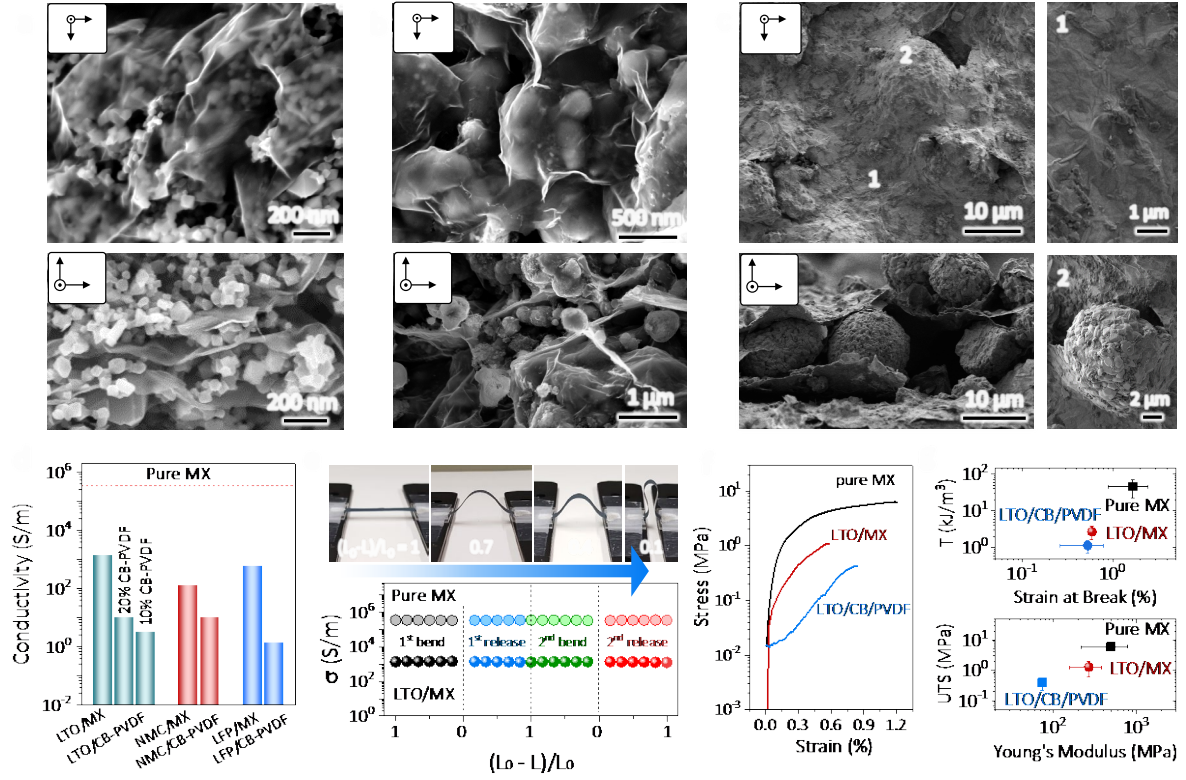


Figure 2. Physical properties of films enabled by MXene inks. Top-view (top panel) and cross-sectional (bottom panel) SEM images of a) LTO/MX, b) LFP/MX and c) NMC/MX electrodes. Higher magnification SEM images of NMC/MX are on the right panel of c. These SEM images indicate that MXene nanosheets form a continuous interconnected metallic network that well wraps active material particles, ensuring excellent charge transport kinetics. d) Electrical conductivity comparison of different electrodes with dual additives or MXene conductive binders. The dashed line is pure filtrated MXene film. e) Electrical conductivity change of the LTO/MX and pure MX freestanding films upon bending. The flat conductivity of bending/releasing degree indicates both film's robust nature. The sample was prepared by filtering LTO/MX slurry to membrane (Celgard 3501). f) Stress-strain curves for LTO/MX and MXene freestanding films. Their tensile toughness (i.e. tensile energy density required to break film) plotted as a function of strain at break (%), as well as UTS plotted as a function of Young's modulus are compared in top and bottom panels in g), respectively.

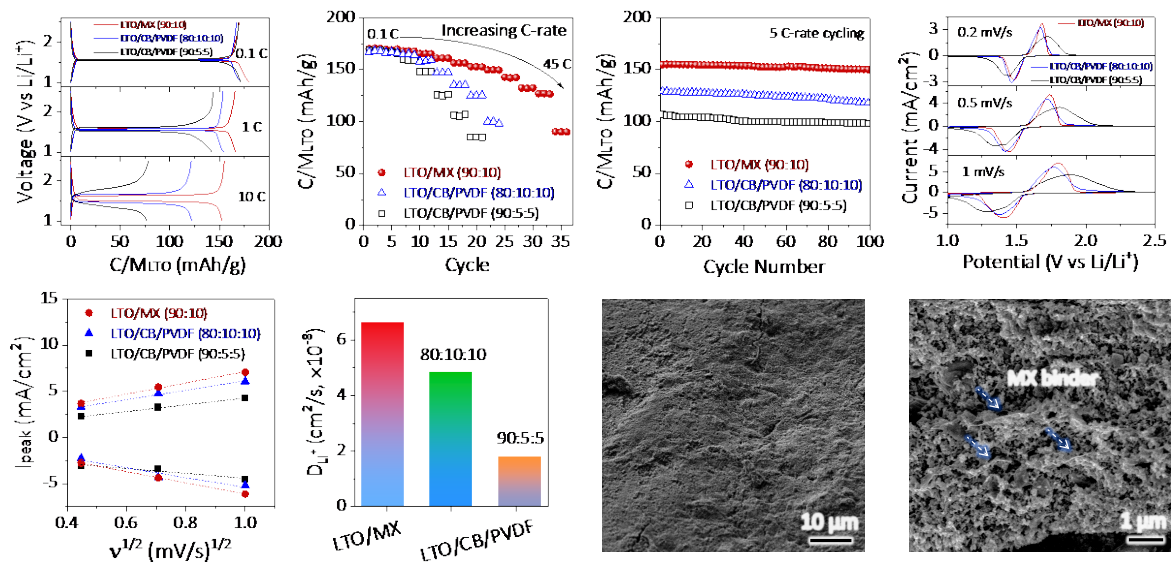


Figure 3. Electrochemical characterizations of LTO/MX anode. a) GCD curves and b) specific capacity of LTO/MX and LTO/CB/PVDF electrodes (with different weight fractions) at different C-rate. The mass loading of LTO/MX is 3.8-4.2 mg/cm². c) Cycling performance of different LTO-based electrodes at 5C. d) CV curves of three electrodes at different scan rates. e) Peak current of different electrodes plotted as a function of $v^{0.5}$. f) Li^+ diffusion coefficient of different electrodes calculated from e). SEM images of the LTO/MX electrode at g) top-view and h) cross-sectional view indicate that MXene conductive binders have been preserved after repeated 100 cycles.

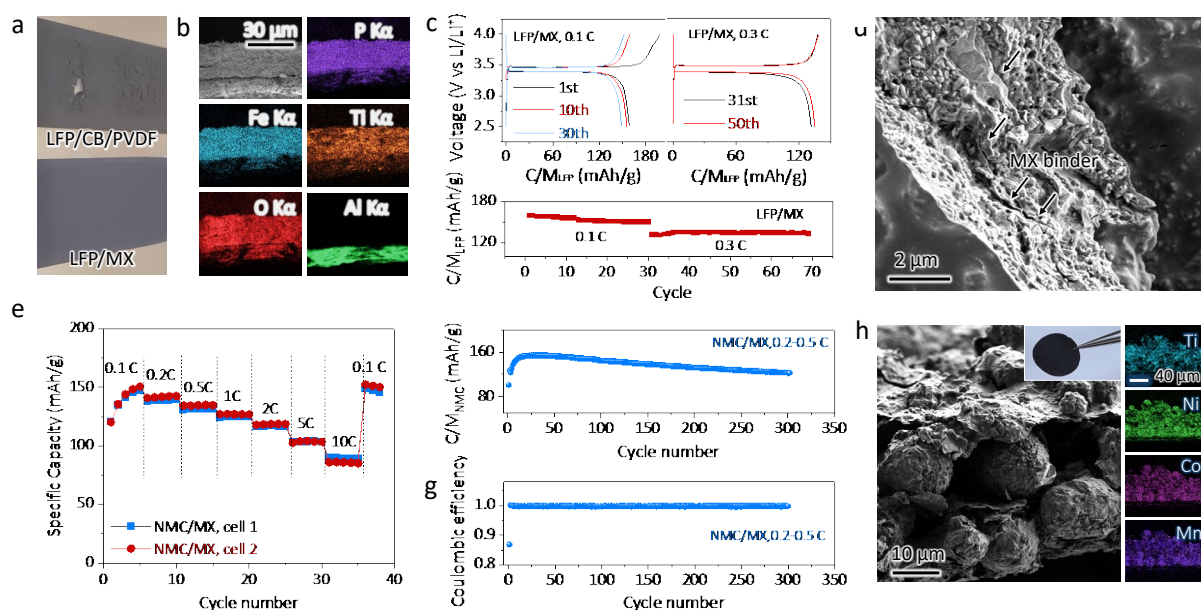


Figure 4. Electrochemical characterizations of LFP/MX and NMC/MX cathodes. a) Optical images of slurry-cast LFP/MX and LFP/CB/PVDF electrodes, showing crack formation in the latter. b) Cross-sectional SEM image of LFP/MX with energy-dispersive X-ray (EDX) mapping. c) GCD curves of LFP/MX at different C-rate (top) with its cycling performance shown in the bottom panel. d) SEM image of LFP/MX after cycling at 0.3 C, showing the presence of MXene nanosheets. e) Rate performance of NMC/MX cathode at different C-rates. The mass loading of the NMC/MX is ~ 3.0 mg/cm². f) Long-term cycling performance of NMC/MX (charging at 0.2 C and discharging at 0.5 C, top panel) and its corresponding Coulombic efficiency (bottom panel). h) Cross-sectional SEM image of NMC/MX after cycling (as seen in the inset) with the EDX mapping shown on the right panel. The homogeneous distribution of different elements indicates that MXene nanosheet network has been well preserved upon repeated charging-discharging.

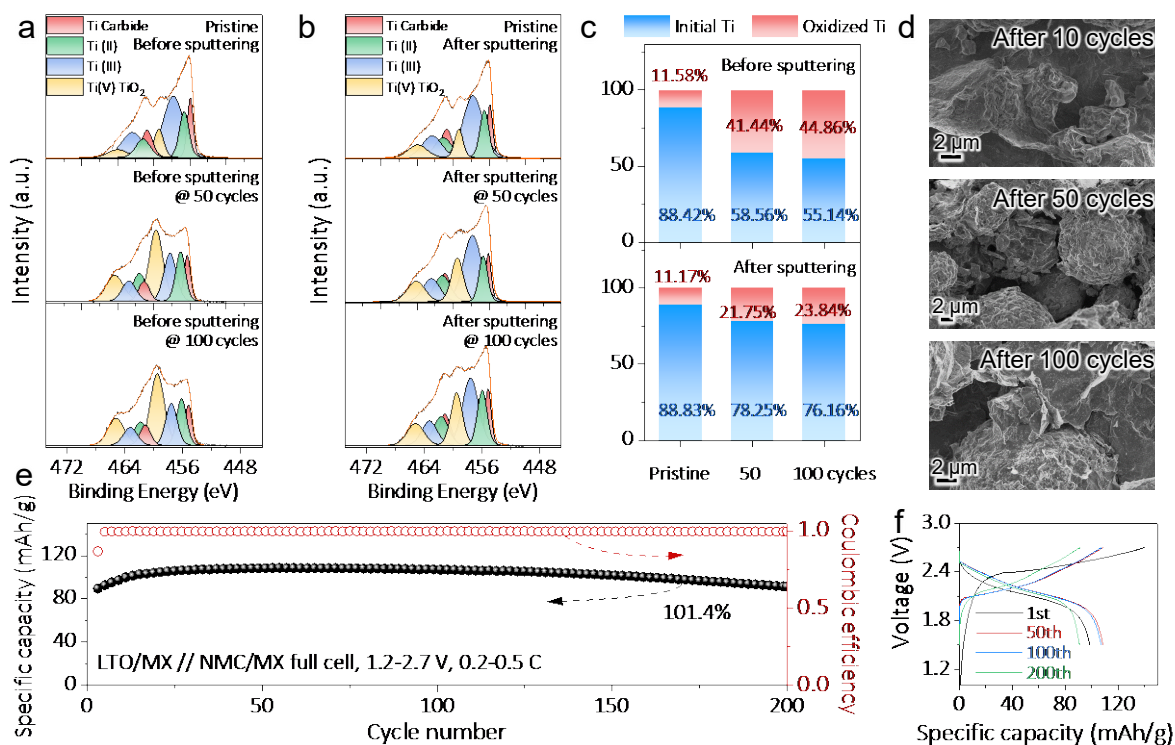


Figure 5. Mechanism analysis of MXene conductive binders for the high-voltage cathode.

- a) Core-level XPS spectra of deconvoluted Ti2p in NMC/MX electrode cycled for different times before Ar⁺ sputtering a) and after Ar⁺ sputtering b). c) Normalized percentage of oxidized Ti to initial Ti under different cycling numbers before (top) and after (bottom) Ar⁺ sputtering. d) SEM images of NMC/MX electrode after cycling for different times. e) Full cell cycling performance and Coulombic efficiency with LTO/MX as anode and NMC/MX as a cathode. f) GCD curves of the assembled full cell at different cycles.

References

1. M. S. Whittingham, *Chem. Rev.* **2014**, *114*, 11414.
2. W. Li, B. Song, A. Manthiram, *Chem. Soc. Rev.* **2017**, *46*, 3006.
3. W. Zhao, L. Zou, L. Zhang, X. Fan, H. Zhang, F. Pagani, E. Brack, L. Seidl, X. Ou, K. Egorov, X. Guo, G. Hu, S. Trabesinger, C. Wang, C. Battaglia, *Small* **2022**, e2107357.
4. W. Zhao, J. Zheng, L. Zou, H. Jia, B. Liu, H. Wang, M. H. Engelhard, C. Wang, W. Xu, Y. Yang, J. G. Zhang, *Adv. Energy Mater.* **2018**, *8*, 1800297.
5. H. Jia, X. Li, J. Song, X. Zhang, L. Luo, Y. He, B. Li, Y. Cai, S. Hu, X. Xiao, C. Wang, K. M. Rosso, R. Yi, R. Patel, J. G. Zhang, *Nat. commun.* **2020**, *11*, 1474.
6. C. K. Chan, H. Peng, G. Liu, K. McIlwrath, X. F. Zhang, R. A. Huggins, Y. Cui, *Nat. nanotechnol.* **2008**, *3*, 31.
7. J. M. T. M. Armand, *Nature* **2001**, *414*, 359.
8. W. Zhao, G. Zhong, M. J. McDonald, Z. Gong, R. Liu, J. Bai, C. Yang, S. Li, W. Zhao, H. Wang, R. Fu, Z. Jiang, Y. Yang, *Nano Energy* **2016**, *27*, 420.
9. H. Zhao, Z. Wang, P. Lu, M. Jiang, F. Shi, X. Song, Z. Zheng, X. Zhou, Y. Fu, G. Abdelbast, X. Xiao, Z. Liu, V. S. Battaglia, K. Zaghib, G. Liu, *Nano Lett* **2014**, *14*, 6704.
10. V. A. Nguyen, C. Kuss, *J. Electrochem. Soc.* **2020**, *167*, 065501.
11. J. Kim, M. S. Kim, Y. Lee, S. Y. Kim, Y. E. Sung, S. H. Ko, *ACS Appl. Mater. Inter.* **2022**, *14*, 17340.
12. S. Gao, F. Sun, N. Liu, H. Yang, P.-F. Cao, *Mater. Today* **2020**, *40*, 140.
13. X. O. Xinming Fan, Wengao Zhao, Yun Liu, Bao Zhang, Jiafeng Zhang, Lianfeng Zou, Lukas Seidl, Yangzhong Li, Guorong Hu, Corsin Battaglia, Yong Yang, *Nat. commun.* **2021**, *12*, 1.
14. J. Li, Y. Cai, H. Wu, Z. Yu, X. Yan, Q. Zhang, T. Z. Gao, K. Liu, X. Jia, Z. Bao, *Adv. Energy Mater.* **2021**, *11*, 2003239.
15. T. M. Higgins, S. H. Park, P. J. King, C. J. Zhang, N. McEvoy, N. C. Berner, D. Daly, A. Shmeliov, U. Khan, G. Duesberg, V. Nicolosi, J. N. Coleman, *ACS Nano* **2016**, *10*, 3702.
16. A. Brilloni, F. Marchesini, F. Poli, E. Petri, F. Soavi, *Energies* **2022**, *15*, 2608.
17. T. Zhu, G. Liu, *J. Electrochem. Soc.* **2021**, *168*, 050533.
18. P. Das, R. Elizalde-Segovia, B. Zayat, C. Z. Salamat, G. Pace, K. Zhai, R. C. Vincent, B. S. Dunn, R. A. Segalman, S. H. Tolbert, S. R. Narayan, B. C. Thompson, *Chem. Mater.* **2022**, *34*, 2672.
19. Y. Shi, X. Zhou, G. Yu, *Accounts Chem. Res.* **2017**, *50*, 2642.
20. O. Gerard, A. Numan, S. Krishnan, M. Khalid, R. Subramaniam, R. Kasi, *J. Energy Storage* **2022**, *50*, 104283.
21. T. Y. Kwon, K. T. Kim, D. Y. Oh, Y. B. Song, S. Jun, Y. S. Jung, *Energy Storage Mater.* **2022**, *49*, 219.
22. S. Vadivel, M. Sawangphruk, *J. Mater. Chem. A* **2020**, *8*, 20714.
23. S. H. Park, P. J. King, R. Tian, C. S. Boland, J. Coelho, C. Zhang, P. McBean, N. McEvoy, M. P. Kremer, D. Daly, J. N. Coleman, V. Nicolosi, *Nat. Energy* **2019**, *4*, 560.
24. M. Yang, F. Qin, W. Wang, T. Liu, L. Sun, C. Xie, X. Dong, X. Lu, Y. Zhou, *J. Mater. Chem. A* **2021**, *9*, 3918.
25. W. Zeng, L. Wang, X. Peng, T. Liu, Y. Jiang, F. Qin, L. Hu, P. K. Chu, K. Huo, Y. Zhou, *Adv. Energy Mater.* **2018**, *8*, 1702314.
26. Y. Luo, R. Guo, T. Li, F. Li, Z. Liu, M. Zheng, B. Wang, Z. Yang, H. Luo, Y. Wan, *ChemSusChem* **2019**, *12*, 1591.
27. I. İ. Avcı Yayla, N. Yuca, E. Sezer, B. Ustamehmetoğlu, *Energy Storage* **2022**, *4*.
28. H. Zhao, Z. Wang, P. Lu, M. Jiang, F. Shi, X. Song, Z. Zheng, X. Zhou, Y. Fu, G. Abdelbast, X. Xiao, Z. Liu, V. S. Battaglia, K. Zaghib, G. Liu, *Nano Lett.* **2014**, *14*, 6704.

29. T. M. Higgins, S. H. Park, P. J. King, C. J. Zhang, N. McEvoy, N. C. Berner, D. Daly, A. Shmeliov, U. Khan, G. Duesberg, V. Nicolosi, J. N. Coleman, *ACS Nano* **2016**, *10*, 3702.
30. T. Zhu, G. Liu, *J. Electrochem. Soc.* **2021**, *168*, 050533.
31. S. Vadivel, M. Sawangphruk, *J. Mater. Chem. A* **2020**, *8*, 20714.
32. P. Das, R. Elizalde-Segovia, B. Zayat, C. Z. Salamat, G. Pace, K. Zhai, R. C. Vincent, B. S. Dunn, R. A. Segalman, S. H. Tolbert, S. R. Narayan, B. C. Thompson, *Chem. Mater.* **2022**, *34*, 2672.
33. B. Anasori, Y. Xie, M. Beidaghi, J. Lu, B. C. Hosler, L. Hultman, P. R. C. Kent, Y. Gogotsi, M. W. Barsoum, *ACS Nano* **2015**, *9*, 9507.
34. M. Naguib, O. Mashtalir, J. Carle, V. Presser, J. Lu, L. Hultman, Y. Gogotsi, M. W. Barsoum, *ACS Nano* **2012**, *6*, 1322.
35. B. Anasori, M. R. Lukatskaya, Y. Gogotsi, *Nat. Rev. Mater.* **2017**, *2*.
36. C. J. Zhang, B. Anasori, A. Seral-Ascaso, S. H. Park, N. McEvoy, A. Shmeliov, G. S. Duesberg, J. N. Coleman, Y. Gogotsi, V. Nicolosi, *Adv. Mater.* **2017**, *29*, 1702678.
37. M. Alhabeb, K. Maleski, B. Anasori, P. Lelyukh, L. Clark, S. Sin, Y. Gogotsi, *Chem. Mater.* **2017**, *29*, 7633.
38. A. Lipatov, H. D. Lu, M. Alhabeb, B. Anasori, A. Gruverman, Y. Gogotsi, A. Sinitskii, *Sci. Adv.* **2018**, *4*.
39. C. J. Zhang, S. H. Park, A. Seral-Ascaso, S. Barwich, N. McEvoy, C. S. Boland, J. N. Coleman, Y. Gogotsi, V. Nicolosi, *Nat. Commun* **2019**, *10*, 849.
40. A. Lipatov, M. Alhabeb, M. R. Lukatskaya, A. Boson, Y. Gogotsi, A. Sinitskii, *Adv. Electron. Mater.* **2016**, *2*, 1600255.
41. C. J. Zhang, L. McKeon, M. P. Kremer, S. H. Park, O. Ronan, A. Seral-Ascaso, S. Barwich, C. O. Coileain, N. McEvoy, H. C. Nerl, B. Anasori, J. N. Coleman, Y. Gogotsi, V. Nicolosi, *Nat. Commun.* **2019**, *10*, 1795.
42. C. J. Zhang, S. Pinilla, N. McEvoy, C. P. Cullen, B. Anasori, E. Long, S.-H. Park, A. Seral-Ascaso, A. Shmeliov, D. Krishnan, C. Morant, X. Liu, G. S. Duesberg, Y. Gogotsi, V. Nicolosi, *Chem. Mater.* **2017**, *29*, 4848.
43. K. B. Hatzell, L. Fan, M. Beidaghi, M. Boota, E. Pomerantseva, E. C. Kumbur, Y. Gogotsi, *ACS Appl. Mater. Inter.* **2014**, *6*, 8886.
44. C. Zhang, K. B. Hatzell, M. Boota, B. Dyatkin, M. Beidaghi, D. Long, W. Qiao, E. C. Kumbur, Y. Gogotsi, *Carbon* **2014**, *77*, 155.
45. S. Barwich, J. N. Coleman, M. E. Mobius, *Soft Matter* **2015**, *11*, 3159.
46. R. Tian, S. H. Park, P. J. King, G. Cunningham, J. Coelho, V. Nicolosi, J. N. Coleman, *Nat. Commun* **2019**, *10*, 1933.
47. K. Tang, X. Yu, J. Sun, H. Li, X. Huang, *Electrochim. Acta* **2011**, *56*, 4869.